DOI 10.24425/aee.2026.158265

Research on torque ripple suppression method of high-speed permanent magnet synchronous generator based on single-phase correction winding

CUNXIANG YANG, XUDONG ZHAO, HONGBO QIU✉, YUNZHUANG WANG

College of Electric and Information Engineering, Zhengzhou University of Light Industry Zhengzhou City, Henan, China

e-mail: ✉ *qiuhongbo@zzuli.edu.cn*

(Received: 03.12.2025, revised: 28.04.2026)

Abstract: To address the torque ripple and consequent vibration induced by inter-turn short-circuit (ITSC) faults in high-speed permanent magnet synchronous generators (HSPMSGs), an HSPMSG incorporating a single-phase correction winding configuration is employed for torque ripple suppression. This particular winding configuration enables effective mitigation of the torque ripple caused by ITSC faults. An analytical magnetomotive force (MMF) model under ITSC fault conditions is established based on the winding topology of a back-wound HSPMSG. Through this model, the critical parameters that govern torque ripple are identified, and torque ripple together with vibration characteristics under ITSC faults are3 experimentally measured on a prototype. Subsequently, a dedicated suppression method for torque ripple is proposed after detailed examination of the ripple components arising from the fault, and the optimal suppression strategy is derived accordingly. Finite element analysis is performed to compare torque ripple and vibration performance before and after the introduction of the correction winding. Results confirm that, upon the occurrence of an ITSC fault, the proposed configuration can effectively suppress torque ripple and significantly reduce vibration levels in the generator.

Key words: high-speed permanent magnet synchronous generators, inter-turn short-circuit faults, single-phase correction winding, torque ripple

1. Introduction

High-speed permanent magnet synchronous generators (HSPMSGs) are increasingly applied in aerospace, medical equipment, and military systems because of their compact structure and high-power density [1]. Their high specific power and efficiency make them attractive for integrated

power units where volume and mass are strictly constrained [2]. In addition, HSPMSGs have been widely adopted in electric spindles, aerospace actuators, precision machine tools, and high-performance compressors to meet the demand for high-speed and high-power-density energy conversion [3]. As these applications continue to push toward higher rotational speed and higher power density, machine reliability is no longer judged only by nominal efficiency and torque quality, but increasingly by the ability to maintain stable operation under incipient faults and avoid catastrophic escalation in tightly integrated systems [4].

Among various failure modes, stator inter-turn short-circuits (ITSC) faults are particularly critical because the local shorted loop can induce a large circulating current, leading to severe localized I^2R loss and rapid thermal deterioration that may escalate to irreversible winding damage within a short time [5]. At the system level, the same fault mechanism also introduces asymmetric magnetomotive force (MMF) that distorts the air-gap field distribution, which can degrade generator output voltages and increase harmonic components – often unacceptable in practical electricity generation systems where power quality and electromagnetic compatibility are strict requirements [6].This reality exposes a key bottleneck in the field: most fault-related studies emphasize detection or post-failure analysis, but there is still a lack of a practical and physically grounded method that can actively reshape the fault-induced electromagnetic excitation to keep the machine mechanically stable during the short but decisive period before shutdown/maintenance. Even when thermal runaway and voltage harmonics are recognized as primary concerns, the electromechanical consequence of ITSC faults – pronounced torque ripple and unbalanced electromagnetic forces – can immediately excite mechanical resonance, aggravate vibration, accelerate bearing wear, and compromise rotor–stator air-gap integrity, especially in high-speed machines where vibration margins are small [7]. Therefore, mitigating fault-induced torque ripple and vibration is not a secondary "comfort feature"; it is a mechanism-level lever that reduces dynamic stress and improves mechanical survivability during fault-tolerant operation. In healthy-condition operation, many torque ripple reduction techniques have been developed through design optimization and electromagnetic shaping, including multi-objective optimization to refine rotor/stator geometry under mechanical constraints [8] and rotor auxiliary slots to reshape the air-gap field and reduce torque pulsation [9]. Magnet skewing, notching, and flux-shaping methods have also been used to suppress cogging torque and improve back-EMF waveform quality [10]. For high-speed PM machines, magnet segmentation is a practical approach to reduce parasitic effects and losses [11], and retention sleeve thickness optimization further balances electromagnetic performance with mechanical strength [12]. Reluctance slots and multi-layer magnet arrangements have been investigated to improve flux distribution and robustness [13], while segmented skew poles and related rotor arrangements have been explored in PM-assisted synchronous reluctance generator/motor topologies to enhance electromagnetic performance [14]. Novel flux-barrier designs and stator slot adaptations have also been reported to reduce high-frequency losses and improve torque characteristics [15].

These studies collectively establish powerful tools for improving torque smoothness in normal operation. Control oriented strategies likewise target ripple suppression under inverter-fed conditions, such as variable-switching-frequency PWM methods [16] and online parameter identification (e.g., recursive least-squares inductance estimation) to improve robustness across operating points [17]. Perfect tracking control has been developed to improve current tracking and torque smoothness [18], and winding arrangement optimization combined with magnet

step-skewing can suppress specific ripple components [19]. Independent multi-winding supply configurations further enhance controllability and fault tolerance in precision applications [20], while parameter-based instantaneous torque estimation and flux-based instantaneous torque estimation have been introduced within advanced control schemes to reduce ripple beyond conventional PI control [21, 22].

However, most existing ripple-reduction methods are developed for healthy operation and are not explicitly designed for the ITSC fault mechanism. Under an ITSC fault, the additional fault-induced MMF interacts with the permanent-magnet fundamental air-gap field and introduces dominant low-order electromagnetic excitation, which appears as pronounced torque ripple and related force harmonics, thereby aggravating vibration and potentially accelerating fault progression. As such, mitigation strategies that act on the fault-induced electromagnetic excitation become particularly relevant for ITSC conditions.

To address this problem, this paper investigates an HSPMSG equipped with a single-phase correction winding. The correction winding injects a controllable MMF that counteracts the dominant fault-induced ripple component, enabling torque-ripple suppression without major changes to the main winding. An analytical MMF-based model is developed to quantify the relationship among the ITSC short-circuit loop effect, correction current magnitude and phase, and torque ripple. The resulting strategy is validated by finite-element analysis and prototype tests, showing reduced torque ripple and reduced vibration under ITSC conditions.

2. Structure of the high-speed permanent magnet synchronous generator

A 2-pole, 36-slot HSPMSG is taken as an example in this paper. The structure of the prototype and the connection diagram of the main winding are shown in Fig. 1. The main parameters of the prototype are listed in Table 1.

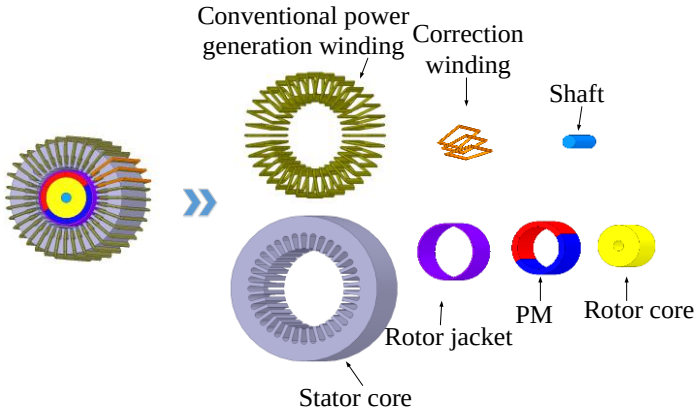

Fig. 1. Three-dimensional structural diagram of the generator

Table 1. Generator structural parameters

Parameters	Value	Parameters	Value
The number of turns of the main winding	5	The number of turns of the correction winding	5
Pole number	2	Winding connection method	Y
Rotor outer diameter (mm)	66	Stator slot fill ratio	68%
Slot number	36	Stator length (mm)	275

The prototype primarily consists of a stator core, permanent magnets, a main winding, and a correction winding. The main winding is symmetrically distributed over the full 360° mechanical angle of the stator, whereas the correction winding is placed in three slots.

The rotor employs a surface-mounted permanent magnet configuration with a rotor jacket to ensure mechanical integrity at high rotational speeds exceeding 20 000 r/min. As shown in Fig. 1, the permanent magnets are evenly segmented and bonded onto the rotor core, providing a nearly sinusoidal air-gap flux distribution for the fundamental component.

The correction winding is concentratively arranged in three consecutive slots within one pole pair and is excited by a controllable current, as shown in Fig. 1. Due to the orthogonal spatial arrangement, the mutual inductance between the main winding and the correction winding is negligible, which enables independent control without compromising the fundamental torque production.

In terms of slot utilization, the stator has 36 slots and the correction winding is associated with three of these slot positions, corresponding to 3/36 of the slot positions. In the prototype, the stator slot fill ratio is 68%, leaving an installation margin in the slot area. During implementation, the correction conductors are accommodated mainly by this available margin and by locally adjusting the conductor size in the corresponding slots while keeping the main-winding turns unchanged. This arrangement allows the correction winding to be embedded while retaining the torque-producing conductors in the same slots. With this arrangement, the proposed configuration introduces minimal additional volume and loss while significantly reducing torque ripple, thereby making the generator suitable for high-performance aerospace servo systems [23].

3. Analysis of torque ripple under ITSC faults

Taking an ITSC occurring in one slot of the phase-A coil as an example, the equivalent circuit model of the stator winding under the ITSC condition is shown in Fig. 2. In the figure, r_A and L_A represent the resistance and inductance of coil A under healthy conditions, respectively; r_X and L_X denote the resistance and inductance of coil X under healthy conditions, respectively; r_{sc} and L_{SC} are the resistance and inductance of the short-circuited loop after the inter-turn short circuit occurs in coil X; r_f is the insulation fault resistance of the stator winding; i_a is the phase-A current; and i_{sc} represents the circulating current in the short-circuit loop.

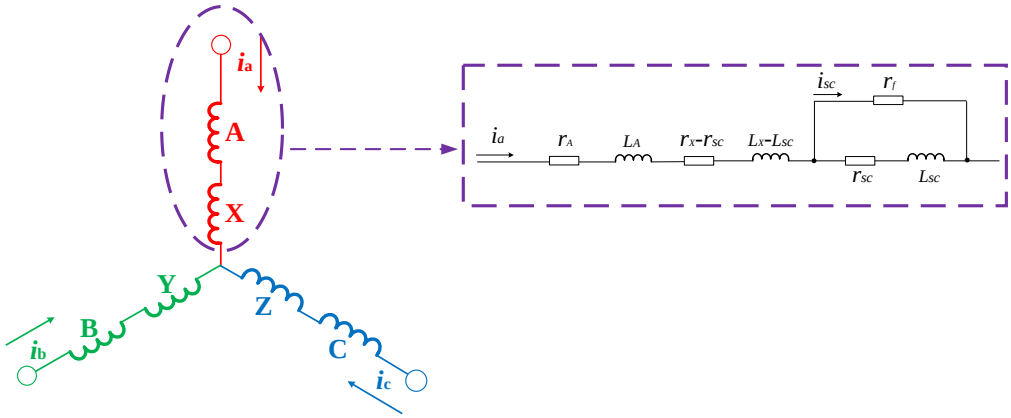

Fig. 2. Equivalent circuit model of the ITSC fault

As shown in Fig. 3, when an ITSC fault occurs, a new closed loop is introduced into the original circuit, giving rise to an additional circulating current in the short-circuit loop [24].

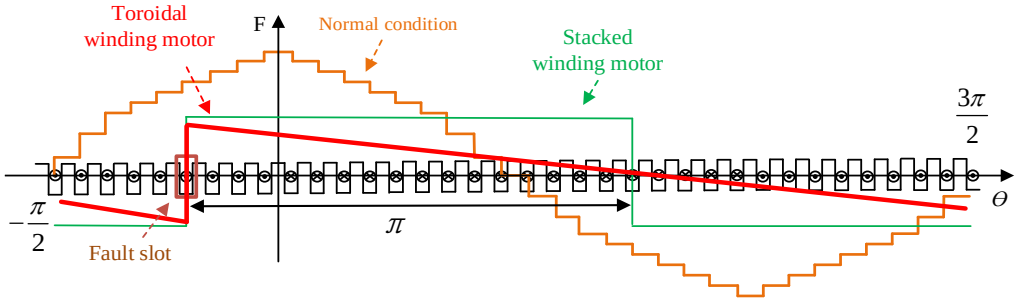

Fig. 3. Comparison of the short-circuit loop magnetomotive force of the GHSPMSG and the magnetomotive force of a conventional winding generator

This current produces an additional magnetomotive force (MMF). The MMF waveform generated by the short-circuit circulating current is subjected to Fourier decomposition, from which the MMF components produced by the short-circuit loop current are obtained. This MMF can be resolved into positive-sequence and negative-sequence components. The positive-sequence component affects only the magnitude of the electromagnetic torque, whereas the negative-sequence component is the primary cause of electromagnetic torque ripple.

The MMF produced by the short-circuit current is presented in Eq. (1) [25].

$$F_{sc}(\theta,t) = \sum_{k=1}^{\infty}\left[\left(\frac{N_{sc}i_{sc}}{\pi k}\sin\frac{k\pi}{2}\right)\cos k\theta + \left(\frac{N_{sc}i_{sc}}{\pi k}\cos\frac{k\pi}{2}\right)\sin k\theta\right]$$
$$= \frac{\sqrt{2}N_{sc}i_{sc}}{2\pi}\sum_{k=1}^{\infty}\frac{1}{k}\left[\cos\left(\omega t - k\theta - \frac{k\pi}{2}\right) - \cos\left(\omega t + k\theta + \frac{k\pi}{2}\right)\right], \quad (1)$$

where F_{sc} is the amplitude of the MMF produced by the circulating current in the short-circuit loop,N_{sc} denotes the number of turns in the short-circuited winding, θ represents the spatial angle, and I_{sc} is the RMS value of the short-circuit loop current, here k takes on the values of 1, 2, 3, etc.

3.1. Mathematical analytical model of electromagnetic torque ripple

The electromagnetic torque acting on the stator is always equal in magnitude and opposite in direction to that acting on the rotor. For an AC generator, the inner bore structure of the stator is relatively simple compared with the rotor, and the arrangement of the stator winding exhibits strong regularity. The torque ripple in the generator under ITSC fault conditions investigated in this paper is caused by the circulating current in the stator short-circuit loop. In this section, an analytical derivation of the electromagnetic torque of the generator under ITSC fault is presented.

During steady-state operation of a three-phase machine, the normal component b_1 of the fundamental air-gap synthetic magnetic field constitutes a rotating magnetic field that travels at synchronous speed. The magnetic flux density is presented in Eq. (2).

$$b_1(\theta, t) = B_1 \sin(\omega t - \theta_s), \tag{2}$$

where B_1 represents the amplitude of the fundamental magnetic field of the air gap.

The operating principle of a HSPMSG is fundamentally based on the law of electromagnetic induction. When the stator winding is energized, the resultant rotating magnetic field interacts with the permanent magnets on the rotor, inducing electromotive force and delivering electrical power. Under healthy operating conditions, the electromagnetic torque is presented in Eq. (3).

$$T_e = \frac{\pi}{2} P^2 F_1 \Phi \sin \delta_1. \tag{3}$$

In the Eq. (3), T_e represents electromagnetic torque, P is the number of pole pairs of the generator, F_1 is the amplitude of the stator fundamental MMF, Φ is the flux of the resultant air-gap magnetic field, and δ_1 is the angle between the fundamental air-gap magnetic field and the stator fundamental MMF.

From the electromagnetic torque expression, it can be seen that, to minimize mechanical vibration and obtain a constant electromagnetic torque without time-varying ripple, both the amplitude F_1 of the stator fundamental MMF and the amplitude of the air-gap fundamental magnetic field B_1 must remain constant, the angle δ_1 between them must also be constant, and no relative motion is permitted between the stator fundamental MMF and the air-gap fundamental field.

When an ITSC fault occurs in the stator winding, a circulating current appears in the short-circuit loop. The MMF produced by this current interacts with the air-gap magnetic field, causing distortion of the field distribution and consequently affecting the torque. Since the permanent magnets are parallel-magnetized, the fundamental component of the air-gap magnetic field is dominant, and the influence of higher-order harmonics can therefore be neglected. The fundamental component c_1 of the short-circuit loop is assumed to lag the air-gap fundamental magnetic field b_1 by an electrical angle ψ_{sc} , which is presented in Eq. (4).

$$c_1 = C_1 \left[\cos\left(\omega t - \theta_s - \frac{\pi}{2} - \psi_{sc}\right) - \cos\left(\omega t + \theta_s + \frac{\pi}{2} - \psi_{sc}\right) \right], \tag{4}$$

where C_1 represents the amplitude of the fundamental wave of the short-circuit loop.

The electromagnetic torque under an ITSC fault is presented in Eqs. (5) to (6).

$$T_{ec} = \frac{\pi}{2} p^2 F_{sc} \Phi \left[\sin\left(\frac{\pi}{2} + \psi_{sc}\right) - \sin\left(2\omega t + \frac{\pi}{2} - \psi_{sc}\right) \right], \tag{5}$$

$$F_{sc} = \frac{\sqrt{2} N_{sc} I_{sc}}{2\pi}, \tag{6}$$

where F_{sc} is the amplitude of the MMF produced by the circulating current in the short-circuit loop.

After the occurrence of an ITSC fault, the electromagnetic torque T_{ec} is primarily generated by the interaction between the fundamental component of the short-circuit loop MMF and the air-gap fundamental magnetic field. The electromagnetic torque comprises a constant component and a ripple component. The constant component has no influence on torque variation, whereas the ripple component, which varies periodically with time at $2\omega t$, causes time-dependent distortion of the magnetic field distribution and consequently gives rise to periodic electromagnetic torque ripple.

3.2. Principle of torque ripple correction

The corrective effect of the single-phase correction winding on electromagnetic torque is illustrated in Fig. 4. When an ITSC fault occurs, the circulating current in the short-circuit loop gives rise to noticeable electromagnetic torque ripple, as shown in Fig. 4(a). By adjusting both the magnitude and phase of the current in the correction winding according to the ITSC fault, an opposing torque component is generated, as depicted in Fig. 4(b). The torque ripple produced by the short-circuit loop under the ITSC fault and the torque ripple produced by the correction winding are then superimposed. As demonstrated in Fig. 4(c), this superposition effectively cancels most of the ripple component, thereby considerably reducing the overall electromagnetic torque ripple.

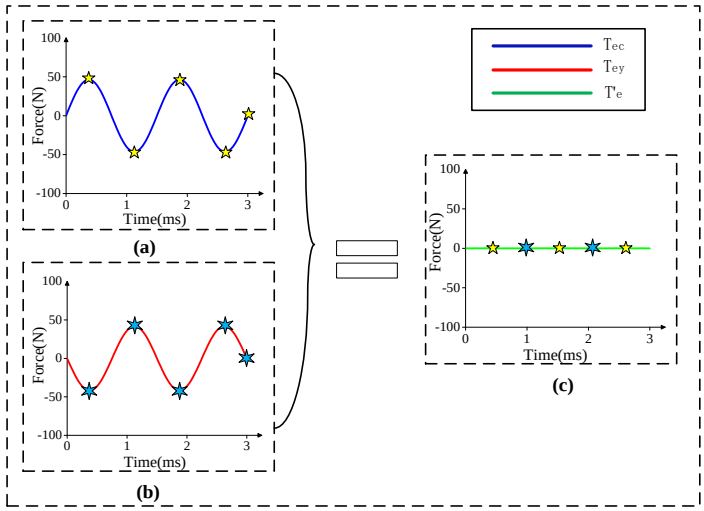

Fig. 4. Torque ripple of the generator under the ITSC fault (a); torque ripple of the generator with the application of the correction winding (b); torque ripple of the generator after correction (c)

3.3. Mathematical correction model of torque ripple

Following the occurrence of an ITSC fault, the magnetic field perturbation induced by the circulating current in the short-circuit loop leads to electromagnetic torque ripple. To thoroughly investigate the influence of fault location on torque performance, three distinct ITSC positions are configured in the stator winding, spatially separated by 120° electrical degrees, as shown in Fig. 5. When the fault occurs, torque ripple is suppressed by appropriately regulating both the magnitude and phase of the correction winding current, thereby enhancing the operational stability of the generator.

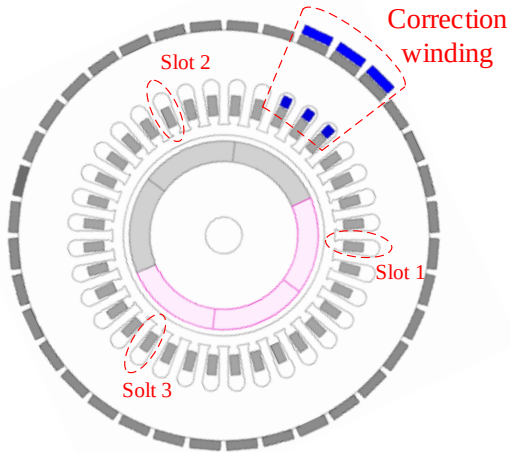

Fig. 5. Topology of the correction winding

The magnetomotive force generated by the correction winding current is presented in Eq. (7).

$$f(x) = \frac{\sqrt{2}N_{yc}I_y}{2\pi}\sum_{k=1}^{\infty}\frac{1}{k}\left[\cos\left(\omega t - kx - \frac{5k\pi}{6} + \psi_y\right) - \cos\left(\omega t + kx + \frac{5k\pi}{6} + \psi_y\right)\right], \quad (7)$$

where N_{yc} denotes the number of turns of the correction winding, I_y and ψ_y represent the amplitude and phase of the corrected winding current.

The electromagnetic torque produced by the interaction between the magnetic field of the correction winding current and the air-gap fundamental magnetic field is presented in Eqs. (8) and (9).

$$T_{ey} = \frac{\pi}{2}p^2F_y\Phi\left[\sin\left(\frac{5\pi}{6} - \psi_y\right) - \sin\left(2\omega t + \frac{5\pi}{6} + \psi_y\right)\right], \quad (8)$$

$$F_y = \frac{\sqrt{2}N_{yc}I_y}{2\pi}, \quad (9)$$

where F_y is the amplitude of the magnetomotive force produced by the correction winding current, T_{ey} represents the electromagnetic torque generated by correcting the winding current.

When an ITSC fault occurs in the generator, the electromagnetic torque with the single-phase correction winding activated is presented in Eq. (10).

$$\begin{aligned} T_e' &= \frac{\pi}{2}p^2F_{sc}\Phi\left[\sin\left(\frac{\pi}{2}+\psi_{sc}\right)-\sin\left(2\omega t+\frac{\pi}{2}-\psi_{sc}\right)\right] \\ &\quad+\frac{\pi}{2}p^2F_y\Phi\left[\sin\left(\frac{5\pi}{6}+\psi_y\right)-\sin\left(2\omega t+\frac{5\pi}{6}-\psi_y\right)\right] \\ &= \frac{\sqrt{2}}{4}p^2\Phi\left\{\begin{array}{c}\left[(N_{sc}I_{sc})\sin\left(\frac{\pi}{2}+\psi_{sc}\right)+N_{yc}I_y\sin\left(\frac{5\pi}{6}-\psi_y\right)\right] \\ \{1\} \\ +\frac{\sqrt{2}}{4}p^2\Phi\left[-N_{sc}I_{sc}\sin\left(2\omega t+\frac{\pi}{2}-\psi_{sc}\right)-N_{yc}I_y\sin\left(2\omega t+\frac{5\pi}{6}-\psi_y\right)\right] \\ \{2\}\end{array}\right\}, \end{aligned} \tag{10}$$

where T_e' represents the electromagnetic torque after the correction of the winding current under inter-turn short circuit fault conditions.

In Eq. (10), the first term {1} does not contain the time variable ωt and represents the DC component of the electromagnetic torque, which is the main factor affecting the increase or decrease of generator power. The second term {2} contains the variable that changes with $2\omega t$ and constitutes the ripple component of the electromagnetic torque. This ripple component is the primary cause of electromagnetic torque ripple and is also the main reason for generator vibration.

When correcting the ITSC fault, it is only necessary to adjust the magnitude I_y and phase ψ_y of the correction winding current so that the second term {2} in Eq. (10) is eliminated and reduced to zero. The electromagnetic torque ripple can be effectively suppressed.

4. Finite element analysis before and after correction

4.1. Finite element simulation and analysis of generator output torque waveforms

The finite-element simulations are performed under the rated operating parameters at the design target speed of 20 000 r/min to assess the fault-induced electromagnetic excitation and the effectiveness of the proposed correction strategy. To evaluate the suppression effect of the single-phase correction winding on torque ripple under ITSC faults, the torque-ripple waveforms of the generator under healthy operation, ITSC fault condition, and with the correction winding activated are presented in Fig. 6.

The variations of torque ripple variation values are shown in Table 2.

Table 2. Variation of torque ripple before and after correction

Harmonic	Normal	Fault	Correction scheme 1	Rate of change	Correction scheme 2	Rate of change
0	14.17	12.91	13.76	6.58%	14.04	8.75%
2	0.005	1.32	0.037	97.2%	0.018	98.6%

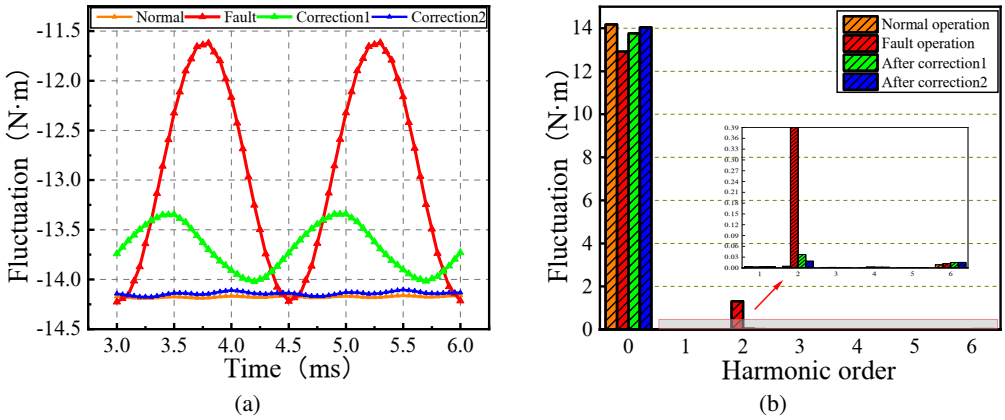

Fig. 6. Torque ripple variation curves before and after correction (a); Fourier decomposition of waveforms before and after correction (b)

As can be seen from Fig. 6, the torque remains stable during healthy operation, with the constant component equal to 14.17 N · m and the ripple component limited to only 0.005 N · m. When an ITSC fault occurs, the torque ripple becomes significantly aggravated: the constant component drops to 12.91 N · m, representing a reduction of 8.89%, while the ripple component increases to 1.32 N · m, which is 1.315 N · m higher than that under healthy conditions and far exceeds the range acceptable for stable generator operation.

To suppress the torque ripple induced by the fault, two correction schemes are proposed in Fig. 6. In Correction Scheme 1, the constant torque component is restored to 13.76 N · m, which is 6.58% higher than that under the faulty condition, while the ripple component is reduced to 0.037 N · m, achieving a suppression rate of 97.2%. In Correction Scheme 2, the suppression effect is further enhanced. The constant component rises to 14.04 N · m, representing an improvement of 8.75% over the faulty state, and the ripple component is dramatically lowered to 0.018 N · m, corresponding to a suppression rate of 98.6%.

Results show that the single-phase correction winding can effectively attenuate the torque ripple caused by ITSC faults and markedly improve the operational stability of the generator. Meanwhile, an ITSC fault reduces the constant component of torque and consequently lowers the output power. The introduction of the correction winding not only suppresses the ripple component but also increases the constant component, thereby partially restoring the output capability of the generator.

4.2. Analysis of the suppression effect of correction winding current on generator torque ripple

To further analyze the correction effects of different schemes on torque ripple are presented in Fig. 7. Figure 7 presents the suppression performance achieved by varying the magnitude and phase of the correction winding current when ITSC faults occur at different positions in the generator winding.

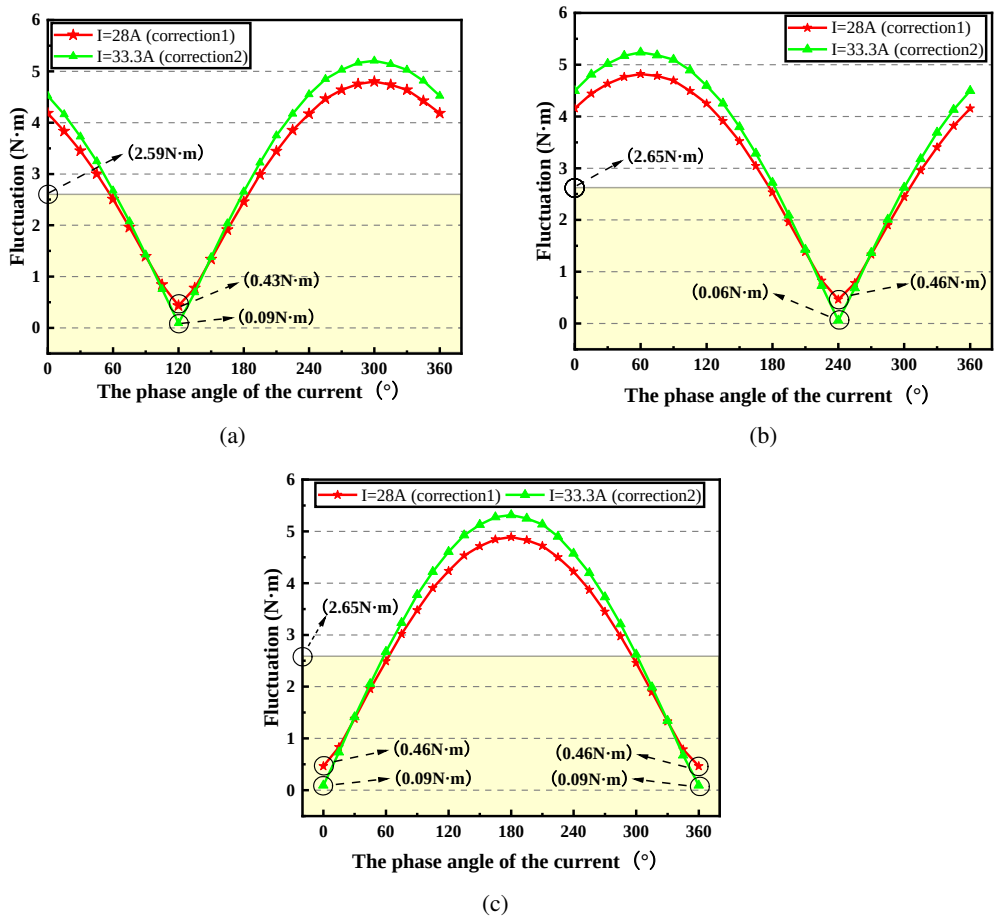

Fig. 7. Suppression effect on torque ripple under ITSC faults at different locations: ITSC fault occurred in the A-phase winding (a); ITSC fault occurred in the B-phase winding (b); ITSC fault occurred in the C-phase winding (c)

Figure 7 shows the torque ripple when ITSC faults occur in slots 1, 2, and 3 of the stator, respectively, with the fault locations indicated in Fig. 5. Under faulty conditions, the torque ripple for each slot stabilizes at approximately 2.6 N · m. After applying Correction Scheme 1, the torque ripple in all three fault cases is reduced to the range of 0.43–0.46 N · m, corresponding to a suppression rate of 82%–83%. With the further implementation of Correction Scheme 2, the torque ripple is decreased to 0.06–0.09 N · m, achieving suppression rates of 96%–98%. The yellow regions in the figures represent the areas where the correction winding exhibits significant suppression effectiveness.

A comprehensive comparison reveals that both correction schemes can substantially suppress the torque ripple induced by the fault, with Scheme 2 providing markedly superior performance. Moreover, in the vicinity of the optimal solution, the suppression effectiveness gradually deteriorates

as the phase of the correction winding current deviates from its optimum value. Therefore, under ITSC fault conditions, the magnitude and phase of the correction winding current must be appropriately selected to ensure optimal torque ripple suppression performance.

4.3. Analysis of the influence of the correction winding on radial electromagnetic force waves

The radial electromagnetic force is subjected to spatial-temporal Fourier decomposition, and the resulting space-time distribution of the radial force waves are shown in Fig. 8. The harmonic spectra of the radial electromagnetic force under both faulty conditions and with the correction winding activated are obtained using the Fourier transform method.

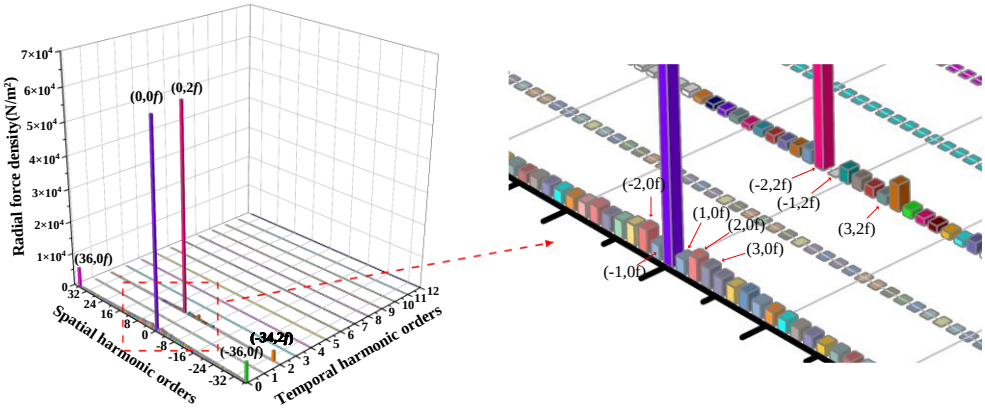

(a) (b)

Fig. 8. Fourier decomposition of radial electromagnetic force waves under generator fault (a); Fourier decomposition of radial electromagnetic force waves under corrected operation of the generator (b)

As shown in Fig. 8, when an ITSC fault occurs, a series of even-multiple spatial harmonics are newly introduced inside the generator, among which harmonics $(\pm 1.0f)$, $(3.2f)$, $(\pm 2.0f)$, $(\pm 3.0f)$, $(-1.2f)$ and $(-2.2f)$ exhibit the most pronounced increase. After the correction winding is activated, these harmonics $(\pm 2.0f)$, $(\pm 3.0f)$, $(-1.2f)$ and $(-2.2f)$ are reduced by 1.65%, 92.61%, 97.07%, and 4.17% respectively. At the same time, the radial electromagnetic force wave $(1.0f)$ increases by 70.66%, and harmonic $(3.2f)$ increases by 71.14%.

It is evident that, with the correction winding in operation, the low-order and $2f$ characteristic radial electromagnetic force waves that are primarily responsible for generator vibration are significantly suppressed, whereas the $0f$ harmonics that do not contribute to vibration are increased. Therefore, the single-phase correction winding can effectively suppress the characteristic radial electromagnetic force waves that cause vibration, thereby reducing the vibration of the generator.

4.4. Analysis of generator exciting force and vibration response

In addition to examining the influence of ITSC faults on torque ripple, analysis of the vibration characteristics of the generator is equally essential. Modal parameters represent a critical index in the evaluation of vibration behavior. When the frequency of the electromagnetic force approaches

a natural frequency of the generator, even a small exciting force can induce severe vibration, which adversely affects the vibration performance of the generator. Consequently, modal analysis of the generator is essential to assess the risk of resonance. The three-dimensional free vibration modes of the stator under free-free boundary conditions are shown in Fig. 9.

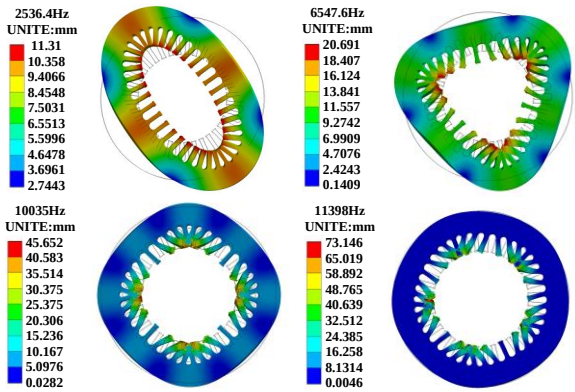

Fig. 9. Three-dimensional free modal analysis of the generator stator

The material parameter of the stator core is listed in Table 3.

Table 3. Material parameters of the stator core

Young's modulus	Poisson's ratio	Stator core density
195 GPa	0.3	7 650 kg/m^3

Under unconstrained conditions, the three-dimensional free modal analysis of the stator is performed, and the second- to fifth-order free modal shapes are obtained, as shown in Fig. 9. When the frequency of the electromagnetic force approaches any of these modal frequencies, intense vibration of the generator will be excited. Therefore, both in the design stage and under fault conditions, electromagnetic force components close to the modal frequencies should be avoided or minimized.

4.5. Analysis of the suppression effect of the correction winding on generator vibration acceleration

The electromagnetic forces are coupled to the tooth surfaces of the stator in the three-dimensional structural model, and finite element harmonic response analysis of the generator electromagnetic vibration is performed. As shown in Fig. 10, the harmonic response comparison before and after fault correction is presented for a constant generator load.

As can be seen from Fig. 10, under healthy operation the vibration acceleration induced by the $2f$, $4f$, and $6f$ components is relatively large. Resonance occurs because the $8f$ frequency is close to the second-order modal frequency of the stator, resulting in a sharp rise of the harmonic

response at $8f$ and a corresponding increase in vibration acceleration. When the ITSC fault occurs, the vibration acceleration at all frequencies increases, with the most pronounced rises observed at $2f$ and $8f$. The amplitude of vibration gradually decreases as the harmonic frequency increases.

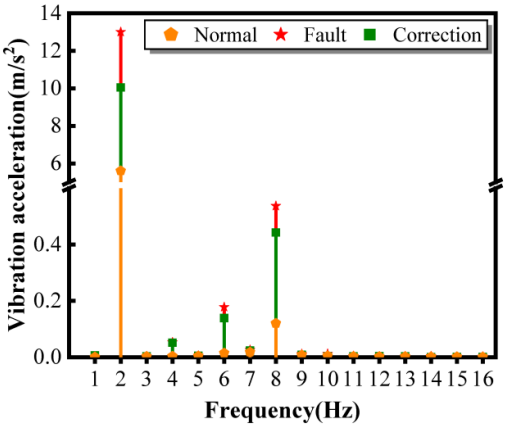

Fig. 10. Comparison of harmonic responses before and after fault under the same load

After the single-phase correction winding is activated, the vibration acceleration at both the $2f$ and $8f$ multiples is markedly reduced, the reduction at $2f$ being particularly significant. These results demonstrate that the correction winding can effectively suppress the vibration of the generator caused by ITSC faults.

4.6. The influence of single-phase correction windings on air-gap flux density

To further examine the effects of single-phase correction windings on generator performance, Fig. 11 shows the generator flux density after the single-phase correction windings act in the case of ITSC fault.

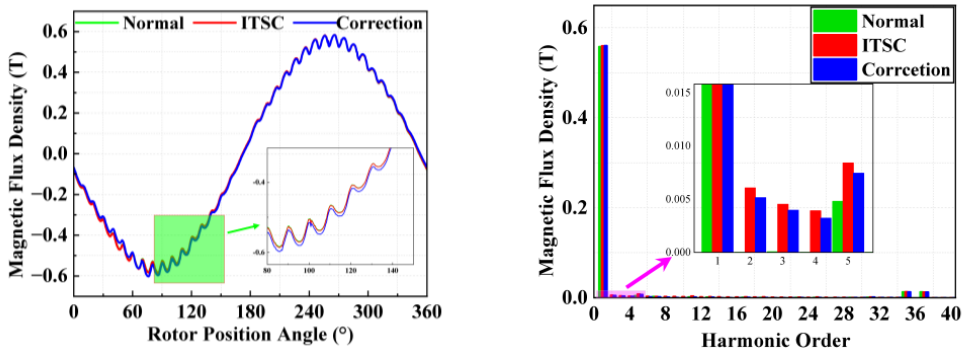

(a) (b)

Fig. 11. The waveform of the air-gap magnetic flux density of the generator after the faulty and corrected winding operation (a) and the result of Fourier decomposition (b)

As shown in Fig. 11, under healthy operation the fundamental component is dominant. When an ITSC fault occurs, a series of odd- and even-order harmonics are introduced, with the 2nd, 3rd, and 4th harmonics exhibiting sharp increases.

After the correction winding is activated, these additional harmonics are reduced – the 2nd harmonic by 15.02%, the 3rd by 12.36%, and the 4th by 17.65%. It is clear that the single-phase correction winding effectively suppresses the radial electromagnetic force harmonics induced by the fault, thereby alleviating magnetic field distortion under faulty conditions.

4.7. The influence of single-phase correction windings on electromagnetic force

To further assess the influence of the single-phase correction winding on generator vibration performance. As shown in Fig. 12, it presents the variation in radial electromagnetic force density before and after correction.

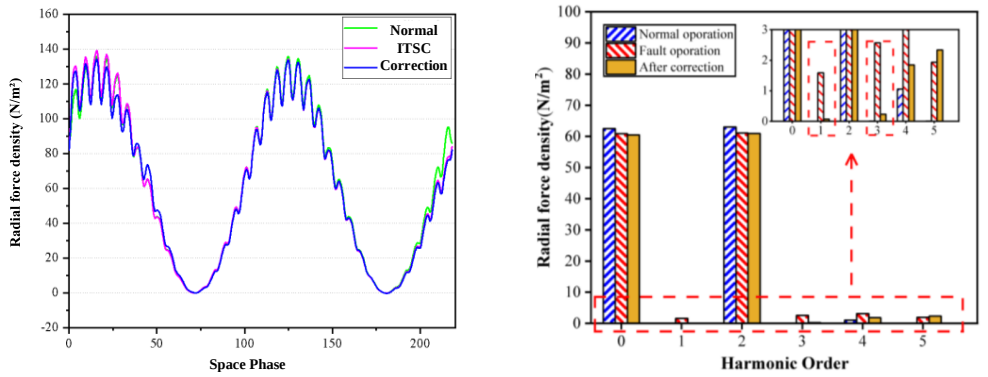

(a) (b)

Fig. 12. Radial electromagnetic force variation curve (a) and its Fourier decomposition (b)

As observed from the figure, upon the occurrence of an ITSC fault, the electromagnetic force distribution within the generator changes substantially, leading to sharp increases in the amplitudes of the 1st- and 3rd-order harmonics.

With the correction winding activated, the perturbed magnetic field distribution is effectively mitigated, resulting in reductions of 30% and 70% in the amplitudes of the 1st- and 3rd-order harmonics, respectively.

These results demonstrate that the single-phase correction winding achieves significant suppression of the fault-induced radial electromagnetic force waves.

5. Experimental validation

5.1. Experimental platform

To verify the effectiveness of the single-phase correction winding, ITSC experiments were conducted. The prototype test platform is shown in Fig. 13. The experimental setup consists of a drive controller, an encoder, the prototype generator, a power analyzer, a DC power supply,

a voltage signal acquisition circuit, a variable resistor, and the prime mover that drives the generator. The drive controller is employed to drive the generator and to regulate the current injected into the correction winding. The variable resistor is used to emulate the contact resistance of the short-circuit loop, while the position sensor provides real-time monitoring of the rotor angular position.

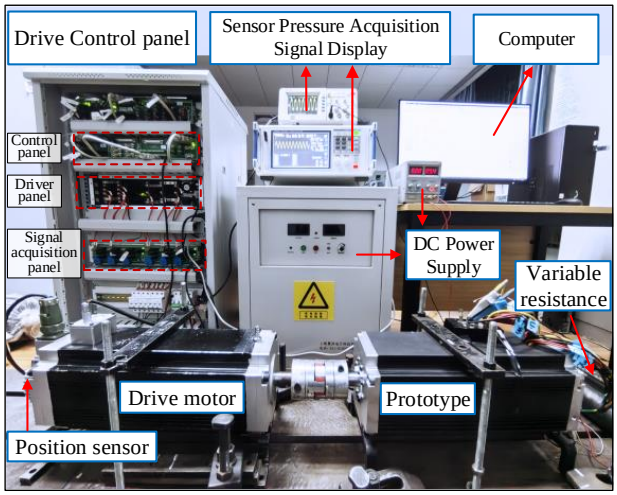

Fig. 13. Prototype testing platform

The winding layout of the prototype is shown in Fig. 14, which includes the main winding, the short-circuited winding, and the correction winding. To simulate ITSC fault experiments, taps are extracted from the coil located in slot 1 of phase A winding. The contact resistance of the fault is realized by external resistors connected in series-parallel configuration, with a fixed resistance value of 0.1Ω. For safety considerations, the generator is tested at a speed of 1 200 rpm throughout the experiments, and the objective is to provide proof-of-concept validation of the proposed electromagnetic excitation suppression mechanism under controlled conditions.

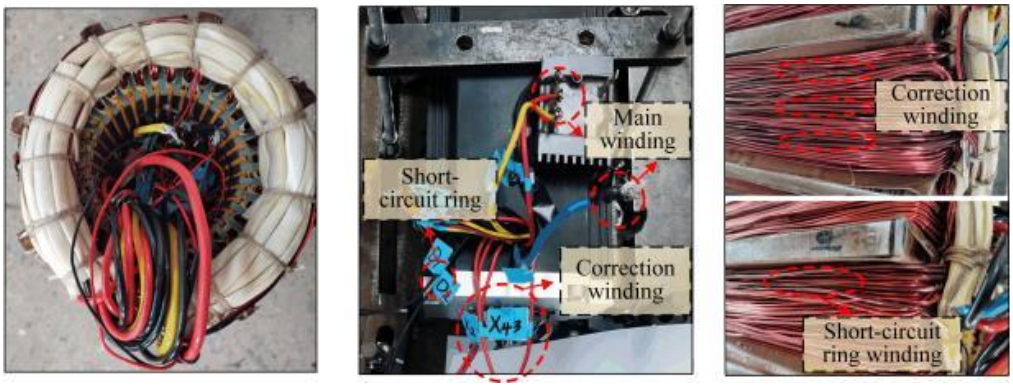

Fig. 14. Winding structure of the prototype

The vibration testing arrangement for the generator is shown in Fig. 15.

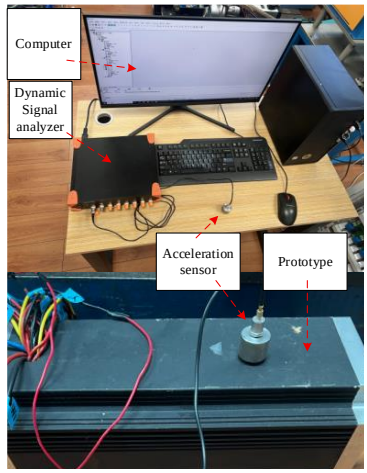

Fig. 15. Dynamic signal analysis system

5.2. Analysis of experimental results

In the experiments, the improvement in vibration characteristics achieved by the proposed correction winding configuration was validated. Vibration response data of the generator under both ITSC fault condition and with the correction winding activated were acquired using acceleration sensors on the test platform, as shown in Fig. 16.

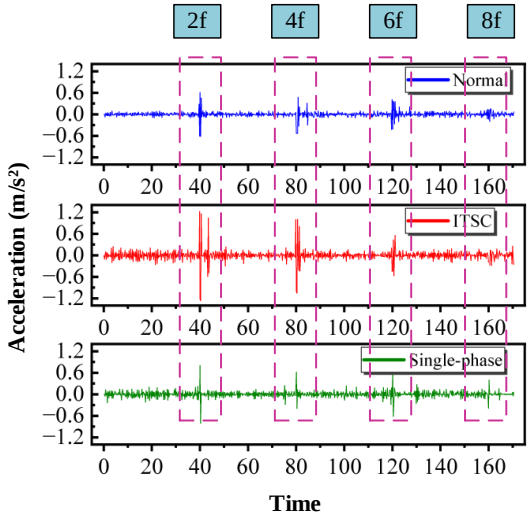

Fig. 16. Vibration testing of the generator stator core before and after correction (acceleration in m/s^2; if recorded in g, 1 g = 9.80665 m/s^2)

The experimental results reveal that, when the ITSC fault occurs, vibration is pronounced across a wide frequency range. After the correction winding is activated, the overall vibration level of the generator decreases noticeably, the peak-to-peak acceleration distribution becomes more uniform, and rotor operation tends toward greater stability. In particular, the vibration acceleration components induced by the harmonic frequencies at $2f$, $4f$, $6f$, and $8f$ are markedly reduced after the correction winding takes effect.

6. Conclusion

A HSPMSG equipped with a correction winding topology is adopted in this study to mitigate the torque ripple caused by inter-turn short-circuit faults, which can aggravate generator vibration and compromise operational stability. Since inter-turn faults are often accompanied by large circulating current and rapid thermal deterioration in the shorted turns, practical fault handling is normally coordinated by protection and thermal management; in this context, the present work provides a mechanism-level approach to suppress the dominant low-order electromagnetic excitation that drives torque ripple and vibration, which is valuable for maintaining mechanical stability within a limited time window before safe shutdown, load transfer, or maintenance. The torque ripple induced by inter-turn short-circuit faults is analyzed through a magnetic-flux-based analytical model, and analytical modeling, finite element analysis at the design target speed of 20 000 r/min, and experimental verification under 1200 r/min for laboratory safety are carried out.

The following conclusions are obtained:

1. After the occurrence of an ITSC fault, the torque ripple component increases from 0.029 N · m to 2.609 N · m, while the average torque decreases from 14.2 N · m to 13.0 N · m. Such deterioration not only undermines the stability of the generator's torque output but also reduces its power generation capability.
2. With the application of the correction winding, the torque ripple component is reduced by 74% and 97.2% in the respective test cases, and the average output torque of the generator is restored to 14.1 N · m. The torque ripple under ITSC conditions is effectively suppressed, thereby improving the generator's output power.
3. Under the action of the correction winding, the radial electromagnetic force wave is increased by 70.66%, and the time–frequency harmonic component at order 2 rises by 71.14%. Correspondingly, the vibration acceleration at the $2f$ and $8f$ frequency multiples is significantly reduced, indicating that the generator vibration is effectively mitigated.

Acknowledgements

This work was sponsored in part by the National Natural Science Foundation of China under Grant 52477066, 52177063, in part by Natural Science Foundation of Henan under Grant 232300421070, and in part by the Program for Science & Technology Innovation Talents in Universities of Henan Province under Grant 23HASTIT026, and in part by the Science and technology project of Henan Province under Grant 232102220080, 222102320074, 242102221002.

References

[1] Lyskawinski W., *Comparative analysis of energy performance of squirrel cage induction motor, line-start synchronous reluctance and permanent magnet motors employing the same stator design*, Archives of Electrical Engineering, vol. 69, no. 4, pp. 967–981 (2020), DOI: 10.24425/aee.2020.134642.

[2] Yang C.X., Wang Y.M., Qiu H.B., *Study on the influence of three-phase voltage unbalance on electromagnetic performance and vibration of high-voltage line-start permanent magnet synchronous motor*, Archives of Electrical Engineering, vol. 74, no. 42, pp. 209–226 (2025), DOI: 10.24425/aee.2025.153020.

[3] Wu S., Sun X., Tong W., *Optimization Design of High-speed Interior Permanent Magnet Motor with High Torque Performance Based on Multiple Surrogate Models*, CES Transactions on Electrical Machines and Systems, vol. 6, no. 3, pp. 235–241 (2022), DOI: 10.30941/CESTEMS.2022.00033.

[4] Zhang D., Liu J., Yi J., Wu T., Yu T., Liu Y., *Design and Torque Ripple Optimization of U-type Permanent Magnet Synchronous Motor*, 2023 26th International Conference on Electrical Machines and Systems (ICEMS), Zhuhai, China, pp. 5058–5063 (2023), DOI: 10.1109/ICEMS59686.2023.10344541.

[5] Qiu H., Zhang H., Li Z., Yang C., *Analysis and Reduction of Unbalanced Magnetic Pull Fluctuation of Gram-Ring-Winding High-Speed Permanent Magnet Generator Based on Correction Winding*, IEEE Transactions on Transportation Electrification, vol. 11, no. 4, pp. 10166–10174 (2025), DOI: 10.1109/TTE.2025.3559188.

[6] Qiu H., Zhang H., Li Z., Huang X., Fu D., Yang C., *Suspension Performance and Fault-Tolerance Principle of High-Speed Permanent Magnet Synchronous Generator*, IEEE Transactions on Energy Conversion, vol. 40, no. 3, pp. 2354–2363 (2025), DOI: 10.1109/TEC.2025.3545758.

[7] Zhou D., Lu L., Yang C., *Optimization of High Speed Permanent Magnet Synchronous Motor Based on Co-simulation Method*, 2023 5th Asia Energy and Electrical Engineering Symposium (AEEES), Chengdu, China, pp. 460–465 (2023), DOI: 10.1109/AEEES56888.2023.10114116.

[8] Sulaiman E., Romalan G.M., Halim N.A., *Skewing and notching configurations for torque pulsation minimization in spoke-type interior permanent magnet motors*, 2016 International Conference on Control, Electronics, Renewable Energy and Communications (ICCEREC), Bandung, Indonesia, pp. 202–207 (2016), DOI: 10.1109/ICCEREC.2016.7814984.

[9] Xu F. *et al.*, *Investigation of Permanent Magnet Segmentations and Gaps in 2-Pole High-Speed Permanent Magnet Motor with Toroidal winding*, 2022 25th International Conference on Electrical Machines and Systems (ICEMS), Chiang Mai, Thailand, pp. 1–6 (2022), DOI: 10.1109/ICEMS56177.2022.9983016.

[10] Yu G., Mu H., Zou J., Tan J., *Design and Optimization of High-Speed Permanent Magnet Synchronous Motors for Electric Spindle Systems*, 2023 IEEE International Conference on Mechatronics and Automation (ICMA), Harbin, Heilongjiang, China, pp. 1918–1923 (2023), DOI: 10.1109/ICMA57826.2023.10215562.

[11] Payza O., Demir Y., Aydin M., *Investigation of Losses for a Concentrated Winding High-Speed Permanent Magnet-Assisted Synchronous Reluctance Motor for Washing Machine Application*, IEEE Transactions on Magnetics, vol. 54, no. 11, pp. 1–5, 8207606 (2018), DOI: 10.1109/TMAG.2018.2848881.

[12] Patel A.N., Kapil A., *Effect of magnet retaining sleeve thickness on cogging torque of radial flux permanent magnet brushless DC motor*, 2016 International Conference on Emerging Trends in Engineering, Technology and Science (ICETETS), Pudukkottai, India, pp. 1–3 (2016), DOI: 10.1109/ICETETS.2016.7603080.

[13] Zhao H., Yu S., Sun F., *Harmonic Suppression and Torque Ripple Reduction of a High-Speed Permanent Magnet Spindle Motor*, IEEE Access, vol. 9, pp. 51695–51702 (2021), DOI: 10.1109/ACCESS.2021.3070010.

[14] Ghasaei A., Vahedi A., *Torque ripple reduction by multi-layering technique in an interior permanent magnet motor used in hybrid electric vehicle*, 2014 International Symposium on Power Electronics, Electrical Drives, Automation and Motion, Ischia, Italy, pp. 372–377 (2014), DOI: 10.1109/SPEEDAM.2014.6871953.

[15] Ismail M.M., Xu W., Liu Y., Dong M., *Improved Torque Ripple Reduction Method for Surface-Mounted Permanent Magnet Synchronous Motor in Flux-Weakening Region*, 2019 22nd International Conference on Electrical Machines and Systems (ICEMS), Harbin, China, pp. 1–6 (2019), DOI: 10.1109/ICEMS.2019.8921942.

[16] Kim S.-J. *et al*., *Torque Ripple Improvement for Interior Permanent Magnet Synchronous Motor Considering Parameters with Magnetic Saturation*, IEEE Transactions on Magnetics, vol. 45, no. 10, pp. 4720–4723 (2009), DOI: 10.1109/TMAG.2009.2022053.

[17] Wang J., Ou J., Yang C., Liu Y., Xu D., *Multi-Variable Structure Optimization for Cogging Torque and Torque Ripple Reduction in High-Speed Permanent-Magnet Motor with Dual-Phase Magnetic Materials*, 2025 IEEE International Conference on Electrical Energy Conversion Systems and Control (IEECSC), Chongqing, China, pp. 127–132 (2025), DOI: 10.1109/IEECSC64206.2025.11099765.

[18] Hossain M.J., Schroeder P., Frankhouse J., McCann R.A., *An Innovative Design of a Permanent Magnet-Assisted Synchronous Reluctance Motor to Improve Torque Performance for High Speed Applications*, 2024 IEEE Energy Conversion Congress and Exposition (ECCE), Phoenix, AZ, USA, pp. 5645–5651 (2024), DOI: 10.1109/ECCE55643.2024.10861378.

[19] Asama J., Yamamoto Y., Oiwa T., Chiba A., *Optimal winding arrangement of a surface-mounted permanent magnet motor for torque ripple reduction*, 2016 IEEE Energy Conversion Congress and Exposition (ECCE), Milwaukee, WI, USA, pp. 1–72016, DOI: 10.1109/ECCE.2016.7855320.

[20] Liu C., Jin S., Zhang F., Wang H., Yao Y., Wang H., *Research on Torque Pulsation Suppression Strategy for High-speed Square-Wave Permanent Magnet Motor*, 2022 25th International Conference on Electrical Machines and Systems (ICEMS), Chiang Mai, Thailand, pp. 1–6 (2022), DOI: 10.1109/ICEMS56177.2022.9983213.

[21] Noguchi S., Fujimoto H., *Torque Ripple Reduction for PMSM based on PWM Pulse Merging Method for High Speed Range*, 2021 IEEE International Conference on Mechatronics (ICM), Kashiwa, Japan, pp. 1–6 (2021), DOI: 10.1109/ICM46511.2021.9385630.

[22] Yukinori Inoue, Shigeo Morimoto, Masayuki Sanada, *Comparative study of IPMSM control strategies for torque ripple reduction*, 2007 European Conference on Power Electronics and Applications, Aalborg, Denmark, pp. 1–9 (2007), DOI: 10.1109/EPE.2007.4417294.

[23] Gul W., Gao Q., Lenwari W., *Optimal Design of a 5-MW Double-Stator Single-Rotor PMSG for Offshore Direct Drive Wind Turbines*, IEEE Transactions on Industry Applications, vol. 56, no. 1, pp. 216–225 (2020), DOI: 10.1109/TIA.2019.2949545.

[24] Qiu H., Zhang H., Li Z., Yang C., *Analysis and Reduction of Unbalanced Magnetic Pull Fluctuation of Gram-Ring-Winding High-Speed Permanent Magnet Generator Based on Correction Winding*, IEEE Transactions on Transportation Electrification, vol. 11, no. 4, pp. 10166–10174 (2025), DOI: 10.1109/TTE.2025.3559188.

[25] Qiu H., Zhang H., Li Z., Huang X., Fu D., Yang C., *Suspension Performance and Fault-Tolerance Principle of High-Speed Permanent Magnet Synchronous Generator*, IEEE Transactions on Energy Conversion, vol. 40, no. 3, pp. 2354–2363 (2025), DOI: 10.1109/TEC.2025.3545758.